4-6-2016

Mass density at geostationary orbit and apparent mass refilling

Richard Denton
Dartmouth College

Kazue Takahashi
Johns Hopkins University

Justice Amoh
Dartmouth College

J. Singer
National Oceanic and Atmospheric Administration Space Weather Prediction Center, Boulder, Colorado

Mass density at geostationary orbit and apparent mass refilling

R. E. Denton[1,2], Kazue Takahashi[3], Justice Amoh Jr[1,2], and H. J. Singer[4]

Justice Amoh Jr., Thayer School of Engineering at Dartmouth, 8000 Cummings Hall, Hanover, NH 03755, USA. (justiceamoh@gmail.com)

R. E. Denton, 32 Oak Tree Dr., New Smyrna Beach, FL 32169, USA. (richard.e.denton@dartmouth.edu)

H. J. Singer, NOAA Space Weather Prediction Center, 325 Broadway, Boulder, CO, 80305, USA. (howard.singer@noaa.gov)

Kazue Takahashi, Johns Hopkins University Applied Physics Laboratory, 11100 Johns Hopkins Rd, Laurel , MD 20723-6099, USA. (kazue.takahashi@jhuapl.edu)

[1]Department of Physics and Astronomy,

Abstract.

We used the inferred equatorial mass density $\rho_{\mathrm{m,eq}}$ based on measurements of Alfven wave frequencies measured by the GOES satellites during 1980–1991 in order to construct a number of different models of varying complexity for the equatorial mass density at geostationary orbit. The most complicated models are able to account for 66% of the variance with a typical variation from actual values of a factor of 1.56. The factors that influenced $\rho_{\mathrm{m,eq}}$ in the models were, in order of decreasing importance, the F10.7 EUV index, magnetic local time, MLT, the solar wind dynamic pressure P_{dyn}, the phase of the year, and the solar wind B_Z (GSM Z direction). During some intervals, some of which were especially geomagnetically quiet, $\rho_{\mathrm{m,eq}}$ rose to

Dartmouth College, Hanover, New Hampshire, USA

[2]Thayer School of Engineering, Dartmouth College, Hanover, New Hampshire, USA

[3]Applied Physics Laboratory, Johns Hopkins University, Laurel, Maryland, USA

[4]National Oceanic and Atmospheric Administration Space Weather Prediction Center, Boulder, Colorado, USA

values that were significantly higher than those predicted by our models. For 10 especially quiet intervals, we examined long-term (> 1 day) apparent refilling, the increase in $\rho_{m,eq}$ at a fixed location. We found that the behavior of $\rho_{m,eq}$ varies for different events. In some cases, there is significant apparent refilling, whereas in other cases $\rho_{m,eq}$ stays the same or even decreases slightly. Nevertheless, we showed that on average $\rho_{m,eq}$ increases exponentially during quiet intervals. There is variation of apparent refilling with respect to the phase of the solar cycle. On the third day of apparent refilling, $\rho_{m,eq}$ has on average a similar value at solar maximum or solar minimum, but at solar maximum, $\rho_{m,eq}$ begins with a larger value and rises relatively less than at solar minimum.

1. Introduction

Mass density controls the time rate of change of magnetohydrodynamic (MHD) processes. It also provides a constraint on composition, that can significantly change the properties of certain waves such as electromagnetic ion cyclotron (EMIC) waves [*Denton et al.*, 2014a]. It also provides a clue about transport of heavy ions, especially O+.

Bulk particle density is difficult to measure using particle instruments because spacecraft charging can shield low energy particles from reaching the particle detector. Because of this, waves are often used to infer the particle density. Plasma wave frequencies can be used to infer the electron density [*Persoon et al.*, 1983; *Benson et al.*, 2004]. And Alfvén wave frequencies are often used to infer the mass density ρ_{m} [*Waters et al.*, 2006; *Denton*, 2006; *Denton et al.*, 2015].

While ideally direct measurements of Alfvén wave frequencies can be used to infer ρ_{m}, often such measurements are lacking, and in that case models are useful to describe the density. *Takahashi et al.* [2010] showed that the single most important parameter predicting magnetospheric mass density is the solar EUV F10.7 index. Greater EUV radiation, as characterized by larger F10.7, leads to larger ρ_{m}. *Denton et al.* [2011] combined this dependence with the variation in ion density measured by the Los Alamos National Lab (LANL) Magnetospheric Plasma Analyzer (MPA) instruments [*Bame et al.*, 1993; *Denton et al.*, 2005] to show that there is a variation in composition over the solar cycle, with significant concentrations of O+ at solar maximum, but low concentrations of O+ at solar minimum. Greater EUV radiation at solar maximum increases the ionospheric temperature, increasing the ionospheric O+ scale height. This combined with greater

wave activity at solar maximum may explain why larger amounts of O+ are able to reach the magnetic equator at geostationary orbit at solar maximum.

Here we will extend the modeling effort of *Takahashi et al.* [2010] and *Denton et al.* [2011] to consider more parameters. This will lead to a model that is more accurate at the expense of being more complicated. In addition we will consider the apparent refilling of ρ_{m} during geomagnetic quiet periods following active periods [e.g., *Denton et al.*, 2012]. *Denton et al.* [2014b] showed that the evolution of the mass density could be very different from that of ion density during these times.

In Section 2, we describe the data used in the study; in Section 3, we present a new model for ρ_{m}; in Section 4, we examine the evolution of ρ_{m} during several quiet events; and in Section 5 we discuss and summarize our results.

2. Data

The set of Alfvén wave frequencies is the same as that used by *Denton et al.* [2015]. These frequencies were measured by magnetometers on Geostationary Operational Environmental Satellites (GOES) at geostationary orbit between 1980 and 1991. For a description of the method to get the mass density, see that of *Takahashi et al.* [2010]. In brief, the wave equation of *Singer et al.* [1981] is solved for the theoretical eigenfrequency given an equatorial value of ρ_{m}, $\rho_{m,eq}$, equal to 1 amu, and the inferred equatorial mass density is found by comparing the observed and theoretical eigenfrequencies using the fact that the frequencies are proportional to the Alfvén speed $\propto 1/\sqrt{\rho_{\mathrm{m}}}$. The TS05 magnetic field model [*Tsyganenko and Sitnov*, 2005] is used with an assumed field line dependence for ρ_{m} as discussed below.

An example of 36 hours of data is shown in Figure 1. The roughly horizontal bands of wave power result from the Alfvén wave harmonics. Note that data gaps occur when Alfvén waves do not occur or where they are difficult to identify because of sporadic (non-banded) occurrence or because of the simultaneous occurrence of broad band wave power such as results from impulsive signals (e.g., at 0500 UT on 11 Feb 1990 in Figure 1).

One difference in method from that of *Takahashi et al.* [2010] is that we use a different model for the field line distribution of ρ_{m}. A power law distribution is assumed for ρ_{m},

$$\rho_{\mathrm{m}} = \rho_{m,eq} \left(\frac{L R_{\mathrm{E}}}{R} \right)^{\alpha}, \tag{1}$$

as has been used by many researchers [*Waters et al.*, 2006; *Denton*, 2006]. Here L is the L shell parameter defined as the maximum geocentric distance to any point on the field line using the TS05 magnetic field model [*Tsyganenko and Sitnov*, 2005] divided by the Earth's radius R_{E}, and α is the power law index. We use a formula for α that is substantially the same as that of *Denton et al.* [2015],

$$\begin{aligned} \alpha \;=\; & 2.06 + 1.24 \cdot \cos\left((\mathrm{MLT} - .15) \cdot 15^{\circ}\right) \\ & + 0.0026 \cdot \mathrm{AE} \cdot \cos\left((\mathrm{MLT} - 0.73) \cdot 15^{\circ}\right) \\ & + 2.1 \cdot 10^{-5} \cdot \mathrm{AE} \cdot \mathrm{F10.7} - 0.010 \cdot \mathrm{F10.7}. \end{aligned} \tag{2}$$

Because this formula depends on F10.7, MLT, and AE, our model results have some small additional dependence on these variables. But this additional dependence is small. As *Denton et al.* [2015] discuss, errors in α could lead to errors in individual ρ_{m} of order 25%. At any rate, use of the statistical model (2) based on data should improve the statistical results for our ρ_{m} model. And hopefully the effect of errors due to incorrect α values will

cancel out in the averaging. The possible effect of field line dependence not described by (1) is more complicated; see the discussion by *Denton et al.* [2006].

A second difference in method is that for each Alfvén frequency, we find $\rho_{\mathrm{m,eq}}$ from the log average value of the value calculated using the observed frequency minus its standard error and that calculated using the observed frequency plus its standard error. Since reduction in frequency leads to a greater proportional change, this shifts the resulting mass densities to slightly higher values than if the peak frequency values were used. The mean value of the difference in the logarithm of the mass density calculated using the measured frequency minus its standard error and that calculated using the measured frequency plus its standard error was 0.20 (corresponding to a factor of $10^{0.20} = 1.6$), and the median value was 0.14 (corresponding to a factor of 1.38).

3. Mass density model

Our process of choosing parameters went through several stages. First we used linear regression and plots of binned quantities using many different solar wind parameters and geomagnetic indices. We eliminated many of these and narrowed down the parameters to the following: the remainder of the fractional year, dYr, indicating season (DOY minus one divided by the number of days in that year); the magnetic local time, MLT, measured in hours; the F10.7 index measured in 10^{-22} W m^{-2} Hz^{-1}, referred to as the solar flux units (sfu, hereinafter); the logarithmic Kp index; the Dst and AE indices measured in nT; the solar wind dynamic pressure P_{dyn} measured in nPa; the solar wind electric field value measured in the GSM Y direction allowing only positive values, $E_{Y\mathrm{s}}$ measured in mV/m; the GSM Z component of the interplanetary magnetic field, B_Z, measured in nT; and the reconnection coupling parameter $d\Phi_{\mathrm{MP}}/dt$ of *Newell et al.* [2007] in units of

$(\mathrm{mV{\cdot}km/(m{\cdot}s)})^{2/3}$. In addition to the instantaneous value of these quantities, we considered averages and extrema of F10.7, Kp, Dst, Ae, P_{dyn}, $E_{Y\mathrm{s}}$, B_Z, and $d\Phi_{\mathrm{MP}}/dt$. The averages were calculated over the previous 3 hours, 6 hours, 12 hours, 24 hours, 48 hours, 96 hours, and 192 hours. The extrema were calculated during the same previous intervals. For Dst, the most negative value was found, while for all other quantities the most positive value was found.

In order to ensure that periodic functions would result from dYr and MLT, we considered dependencies on $\sin(\mathrm{dYr} \cdot 360°)$, $\cos(\mathrm{dYr} \cdot 360°)$, $\sin(\mathrm{MLT} \cdot 15°)$, $\cos(\mathrm{MLT} \cdot 15°)$, rather than directly on dYr and MLT.

Solar wind parameters were taken from the *Kondrashov et al.* [2014] database, which is an improvement over the Qin Denton database [*Qin et al.*, 2007]. The database includes quality factors for P_{dyn} and B_Z, which range from a value of 0 for a parameter that is far from a measured value to 2 for a parameter that is directly measured. A value of at least 1 means that the quantity is not far from measurements and is significantly better than an average value. But even the 0 quality factor values are improved due to Kondrashov et al.'s technique. To get quality factors for the averages and extrema, we averaged the quality factors over the corresponding interval. For E_Y and $d\Phi_{\mathrm{MP}}/dt$, that are calculated from other quantities, the minimum quality factor of the individual quantities was used. But note that E_Y and $d\Phi_{\mathrm{MP}}/dt$ did not end up in any of our formulas; the other quantities were sufficient to account for the amount of variation that could be explained.

Then we used the Eureqa nonlinear genetic regression software [*Schmidt and Lipson*, 2009] to find potential mathematical models for $\log_{10}\rho_{\mathrm{m,eq}}$, minimizing the squared deviation from the observed values. Each data point was weighted by the inverse of the

difference in the logarithm of the mass density calculated using the measured frequency minus its standard error and that calculated using the measured frequency plus its standard error; but this weight was limited to a value of 2.5 (corresponding to a $\log_{10}$ difference of 0.4). (We might have weighted the data using the square of this quantity. We made this choice as a compromise between weighted and non-weighted least-squares.) For this stage of the modeling, we required that the solar wind parameters used in the model, and some selected averages that commonly occur in models, have at least a quality factor of 1.

Eureqa gives a family of formulas of different complexity. For each level of complexity, it gives the formula that best fits the data. We will present several different models of increasing complexity. After finding the form of a particular model from Eureqa, we tuned the parameters using linear or nonlinear minimization for the weighted squared error. This procedure was used because Eureqa often included only the sine or cosine of dYr or MLT in the formula, and we consider the formula no more complicated to use both the sine and cosine, that is, a general phase. Also we used a slightly different data set for this stage of the process; we did not screen the data for high quality values for quantities not used in the modeling. We estimated the error of the formula in the following way. We split the data into intervals of 2 weeks and divided the data in these intervals into five groups. For each group, we calculated the parameters of the model using the other four groups of data, and found the standard error of the resulting model for predicting the observed values of $\log_{10} \rho_{\mathrm{m,eq}}$ for that group. Then we averaged the squared deviations for the five groups of data and took the square root to get the final standard error for the model. Thus the error is calculated using data other than that used for the model. While

this procedure is the best for getting an estimate of the error, the results were not greatly different from using the entire data set, probably because we had a very large amount of data.

The simplest possible model is just the average. The weighted average value of $\log_{10}\rho_{\mathrm{m,eq}}$ yields

$$\log_{10}\rho_{\mathrm{m,eq}} = 1.02, \tag{3}$$

corresponding to $\rho_{\mathrm{m,eq}} = 10^{1.02} = 10.5$ amu/cm^3, and the unbiased weighted standard error calculated in the manner described above is 0.34 corresponding to a variation of a factor of $10^{0.34} = 2.17$. This result is itself interesting. The typical variation from the mean is not large.

For $1.7 < L < 3.1$, *Berube et al.* [2005] found $\log_{10}\rho_{\mathrm{m,eq}} = -0.65L + 5.1$ for -9 nT $< Dst <$ -3 nT and $\log_{10}\rho_{\mathrm{m,eq}} = -0.74L + 5.5$ for $Dst <$ -100 nT. Extrapolation of this formula to $L = 6.8$, a typical value for GOES spacecraft that are slightly off the magnetic equator, yields $\log_{10}\rho_{\mathrm{m,eq}} = 0.68$ for -9 nT $< Dst <$ -3 nT and $\log_{10}\rho_{\mathrm{m,eq}} = 0.47$ for $Dst <$ -100 nT. These values are higher than that in (3), so not surprisingly the unbiased weighted standard error using these formulas is larger, 0.48. Berube et al.'s average $\log_{10}\rho_{\mathrm{m,eq}}$ value might be lower due to a steep L dependence within $1.7 < L < 3.1$ caused by mass loading at the low L shells owing to their close proximity to the ionosphere.

The next simplest model involves just F10.7.

$$\log_{10}\rho_{\mathrm{m,eq}} = 0.088\sqrt{\mathrm{F10.7}_{96}}, \tag{4}$$

where $\mathrm{F10.7}_{96}$ is the average of the F10.7 index over the previous 96 hours. The unbiased weighted standard error is 0.25 corresponding to a variation of a factor of $10^{0.25} = 1.77$.

This formula shows that $\rho_{\mathrm{m,eq}}$ increases with respect to F10.7 as expected from previous studies [*Takahashi et al.*, 2010]. The formula using the square root is slightly more accurate than one using a linear term.

Takahashi et al. [2010] found $\log_{10}\rho_{\mathrm{m,eq}} = 0.42 + 0.0039\mathrm{F10.7}$ using 27 day median values and *Denton et al.* [2011] found $\log_{10}\rho_{\mathrm{m,eq}} = 0.51 + 0.0036\mathrm{F10.7}$ for the yearly median $\rho_{\mathrm{m,eq}}$ using the yearly average of F10.7. Using these formulas with $\mathrm{F10.7}_{96}$ (the preferred average for our instantaneous $\rho_{\mathrm{m,eq}}$ values), we find for our data set unbiased weighted standard errors of 0.26 and 0.25, respectively, which are essentially the same as the value 0.25 for (4).

The simplest formula that includes MLT dependence is

$$\log_{10}\rho_{\mathrm{m,eq}} = 0.088\sqrt{\mathrm{F10.7}_{96}} + 0.17\cos\left((\mathrm{MLT} - 15.6)\cdot 15^{\circ}\right). \quad (5)$$

The unbiased weighted standard error is 0.22 corresponding to a variation of a factor of $10^{0.22} = 1.66$. The MLT dependence peaks at mid afternoon local time.

The simplest formula that includes explicit solar wind forcing is

$$\log_{10}\rho_{\mathrm{m,eq}} = 0.27 + 0.0042\mathrm{F10.7}_{96} + 0.18\cos\left((\mathrm{MLT} - 15.5)\cdot 15^{\circ}\right) + 0.059P_{\mathrm{dyn,12}}, \quad (6)$$

where $P_{\mathrm{dyn,12}}$ is the average of the dynamic pressure over the previous 12 hours. The unbiased weighted standard error is 0.21 corresponding to a variation of a factor of $10^{0.21} = 1.61$. This shows that recently higher dynamic pressure leads to increased mass density.

The most complicated formula that we found "recommended as a solution" by Eureqa (after running the program for several days with 14 processors) is

$$\begin{aligned}\log_{10}\rho_{\mathrm{m,eq}} \;=\; & 0.32 + 0.0038\mathrm{F10.7}_{96} + 0.14\cos\left((\mathrm{MLT} - 13.0)\cdot 15^{\circ}\right) \\ & + 0.054P_{\mathrm{dyn,12}} + 0.07\cos\left((\mathrm{dYr} - 0.053)\cdot 360^{\circ}\right) + 0.016B_{z,3}\end{aligned}$$

$$+13\cos\left((\mathrm{MLT}-18.4)\cdot 15^\circ\right)/\mathrm{F10.7}_{192}, \quad (7)$$

where dYr is remainder of the fractional year, $B_{z,3}$ is B_z averaged over the previous 3 hours, and $\mathrm{F10.7}_{192}$ is the average of the F10.7 index over the previous 192 hours. The terms are ordered roughly in order of their importance. The unbiased weighted standard error is 0.19 corresponding to a variation of a factor of $10^{0.21} = 1.56$. The dYr dependence peaks at about January 20, that is, at the winter solstice. The mass density increases for positive $B_{z,3}$. The simpler MLT dependence in (5) peaking at MLT = 15.6 is now divided into two terms, one peaking at MLT = 13.1, and a second F10.7 dependent term peaking at MLT = 18.1. So the peak in $\rho_{\mathrm{m,eq}}$ is weaker and shifts from dusk toward noon local time at large F10.7, which is characteristic of solar maximum.

There are diminishing returns as one goes to a more complicated model. Using just F10.7, we can decrease the standard error of $\log_{10}\rho_{\mathrm{m,eq}}$ from 0.34 to 0.25. Adding MLT and $P_{\mathrm{dyn},12}$ gets us down to 0.21. Adding dYr, $B_{z,3}$, and $\mathrm{F10.7}_{192}$ in the most complicated model only decreases the standard error of $\log_{10}\rho_{\mathrm{m,eq}}$ from 0.208 for (6) to 0.197. Nevertheless, we do not consider even (7) to be excessively difficult to implement. Using just F10.7, we can account for 45% of the variance (square of the standard error) of $\log_{10}\rho_{\mathrm{m,eq}}$. Using the most complicated formula (7), we can account for 66% of the variance.

In a not totally successful effort to model apparent refilling (to be described below), we added dependence on the average of Kp during the preceding 12 and 48 hours, Kp_{12} and Kp_{48}, respectively. Figure 2a shows as a blue curve the binned values of $\rho_{\mathrm{m,eq}}$ divided by the weighted log average of $\rho_{\mathrm{m,eq}}$, $\rho_{\mathrm{m,eq,av}}$, versus Kp_{12}, the average of Kp over the preceding 12 hours. The total weight of data points in each bin of width 0.2 is shown in Figure 2b. For the vast majority of data points with Kp_{12} values near 2 (Figure 2b), the

dependence of $\rho_{\mathrm{m,eq}}/\rho_{\mathrm{m,eq,av}}$ on Kp_{12} is very small. Because of this, including dependence on Kp_{12} does not greatly affect our model for $\log_{10}\rho_{\mathrm{m,eq}}$ in a statistical sense. But we hoped that it would affect the small number of data points with small Kp_{12}, for which $\rho_{\mathrm{m,eq}}/\rho_{\mathrm{m,eq,av}}$ departs significantly from unity. We modeled the average dependence of $\log_{10}\rho_{\mathrm{m,eq}}$ using a polynomial of order 3, $P_{12}\left(Kp_{12}\right)$, yielding the red curve in Figure 2a. Similarly Figure 2c and d shows the same quantities but using Kp_{48}. More quantities were tried, but these two quantities ended up having the largest coefficients in the modeling expansion. (Values of maximum Kp over the preceding time period yielded a similar dependence to that shown in Figure 2a and c.)

Our formula including $P_{12}\left(Kp_{12}\right)$ and $P_{48}\left(Kp_{48}\right)$ is

$$\begin{aligned}\log_{10}\rho_{\mathrm{m,eq}} \;=\; & 0.32 + 0.0038\mathrm{F10.7}_{96} + 0.14\cos\left((\mathrm{MLT}-12.7)\cdot 15^{\circ}\right) \\ & +0.055P_{\mathrm{dyn},12} + 0.07\cos\left((\mathrm{dYr}-0.050)\cdot 360^{\circ}\right) + 0.015B_{z,3} \\ & +13\cos\left((\mathrm{MLT}-18.5)\cdot 15^{\circ}\right)/\mathrm{F10.7}_{192} \\ & +0.50P_{12}\left(Kp_{12}\right) + 0.20P_{48}\left(Kp_{48}\right), \end{aligned} \tag{8}$$

where the polynomials

$$P_{12}\left(x\right) = -0.00853x^3 + 0.119x^2 - 0.444x + 0.45 \tag{9}$$

$$P_{48}\left(x\right) = -0.0122x^3 + 0.177x^2 - 0.719x + 0.82. \tag{10}$$

The unbiased weighted standard error for (8) is 0.19 corresponding to a variation of a factor of $10^{0.19} = 1.55$. This is not significantly different statistically from that of (8), but includes Kp dependence.

As an example, we show in Figure 3 $\rho_{\mathrm{m,eq}}$ inferred from Alfvén waves measured by GOES 7 (thick blue curves) and that given by the most detailed model without Kp dependence

(7) (solid red curves) and the model with Kp dependence (8) (dotted red curves) during 1991 versus day of year (DOY). This year was at solar maximum and was geomagnetically very active. The model describes well the daily MLT dependence and captures some of the longer timescale variation. Note, for instance the variation in ρ_{m} between day of year (DOY) 100 and 130. In this case, there is not much difference between the two models (solid and dotted red curves).

To better understand the causes of the variation between DOY 100 and 130, we plot in Figure 4 the mass density along with the instantaneous values of the geomagnetic indices and solar wind parameters described above for this time period. Between about DOY 106 and DOY 130, there is a roughly sinoidal oscillation in $\rho_{\mathrm{m,eq}}$. This variation is caused mainly by an oscillation in F10.7 measured at the Earth's surface (Figure 4b) with a very small contribution from a similar oscillation in B_Z (Figure 4i). The period of this oscillation is roughly the period of a solar rotation (27 days as observed), and the variation is probably due to rotation of coronal hole structure on the Sun. This shows that relatively low F10.7 is not necessarily confined to solar minimum. The smaller peak in $\rho_{\mathrm{m,eq}}$ between DOY 115 and 117 is caused mainly by the peak in the dynamic pressure P_{dyn} (Figure 4f) with a smaller contribution from the peak in B_Z (Figure 4i).

Figure 5 is similar to Figure 3, but showing the variation of $\rho_{\mathrm{m,eq}}$ during 1988. This is a quieter year and there is not as much variation other than the daily MLT variation. The model describes most of the variation in the observed $\rho_{\mathrm{m,eq}}$, but there are some deficiencies. Note for instance the large inferred values of $\rho_{\mathrm{m,eq}}$ between DOY 25 and 40 (blue curves) that are not reproduced by the model (red curves).

In order to examine the causes of the evolution of $\rho_{\mathrm{m,eq}}$ during this time, we plot in Figure 6 the mass density and geomagnetic indices and solar wind parameters between DOY 25 and 40 in the same format as Figure 4. The large densities appear to be correlated with low geomagnetic activity as indicated by low Kp, AE, and P_{dyn}. (Low values of $E_{Y\mathrm{s}}$ and $d\Phi_{\mathrm{MP}}/dt$ also occur at the time of the large $\rho_{\mathrm{m,eq}}$ values, but low values of these quantities also occur when $\rho_{\mathrm{m,eq}}$ is relatively small, such as at DOY $\sim$ 20.) These conditions appear to be what we would normally associate with refilling. And note the gradual increase in the inferred value of $\rho_{\mathrm{m,eq}}$ between DOY 22 and 26.

The model with Kp dependence does yield larger values of $\rho_{\mathrm{m,eq}}$ than does the model without Kp dependence (comparing the dotted and solid red curves in Figure 6a), but the Kp dependence is not strong enough to bring the Kp-dependent model (dotted red curve) up to the level of the inferred mass density (blue curves). We tried arbitrarily increasing the coefficients of the polynomial terms in (8), but in that case the model mass density is too high in other regions. Perhaps a more sophisticated technique incorporating the historical record of geomagnetic activity could be used [e.g., *Kondrashov et al.*, 2014] to get better agreement.

4. Mass density refilling

Here we examine the apparent refilling of $\rho_{\mathrm{m,eq}}$ in more detail. Note that what we are calling refilling may not be refilling of a particular flux tube. Rather it is the observed change in $\rho_{\mathrm{m,eq}}$ at the location of the spacecraft versus time. Because the plasma does not necessarily co-rotate with the Earth, we may at different times be sampling plasma on different drift paths. Our best measure of apparent refilling will be the variation from day to day at the same MLT location. Even in that case, the convection may evolve from

day to day so that the observed plasma is not on the same drift path, but we are more likely to be sampling similar plasma if we examine the variation from day to day.

We looked for events with low geomagnetic activity as indicated by Kp of no more than 1.33 (when interpolated to an hourly value) for at least 2 days. We further required that in the hour preceding this quiet intervals, the average of Kp during the previous 12 hours had to be at least 1.75. This second criterion was so that we would have a shift from a more active time to a very quiet time. We found 10 intervals during 1980 to 1991 meeting these criteria and with inferred $\rho_{\mathrm{m,eq}}$ data extending at least 2 days. Figure 7 shows the Kp values for these events versus hour after the start of the low Kp period for the 10 events ordered with respect to F10.7 so that the event with lowest F10.7 (corresponding to solar minimum) is at the top of the figure in Figure 7a, while the event with the highest value of F10.7 (corresponding to solar maximum) is at the bottom of the figure in Figure 7k.

Figure 8 shows the inferred equatorial mass density at GOES (colored symbols and curves) and model mass density using (7) (solid light gray curves) and (8) (dotted light gray curves) versus hours after onset of low Kp for each of the events shown in Figure 7. The elaborate system of symbols (described in the figure caption) enables one to know the location of the spacecraft in MLT and to compare the mass density at a particular location to that at the same location on following days. For instance, the red squares show $\rho_{\mathrm{m,eq}}$ at MLT = 12 hr. By comparing the consecutive red squares from day to day, we can observe the apparent refilling at MLT = 12 hr. First, note that $\rho_{\mathrm{m,eq}}$ is generally higher at solar maximum (bottom panels in Figure 8) than at solar minimum (top panels in Figure 8) due to the F10.7 dependence of $\rho_{\mathrm{m,eq}}$ (in (4), for instance).

Some of the events in Figure 8 exhibit what appears to be refilling. Most notable among these are the ones shown in Figure 8b, c, f, and i. Apparent refilling can lead to $\rho_{m,eq}$ values significantly above that of our model (light gray curves in Figure 8). On the other hand some of the events do not seem to exhibit refilling at all. These include the events shown in Figure 8a, g, and j. In the other three events, there is only slight evidence of refilling. Thus it appears that apparent refilling is not as common for mass density as for electron density. (In the case of electron density, there are also quiet periods when the electron density does not appear to refill [*Denton et al.*, 2012], but such cases appear to be more frequent for $\rho_{m,eq}$.)

Based on these results, it is clear that $\rho_{m,eq}$ does not behave the same for all quiet intervals. However, in order to develop some intuition about the average behavior, we take the log average of all data in four time intervals, the 24 hr interval preceding the onset of low Kp and the first, second, and third 24 hr intervals following the onset of low Kp. The results are shown in Figure 9. The black curve with circles shows the log average of all the data. For the day preceding the period of low Kp and the first day after the onset of low Kp (first two data points in Figure 9), these values are very close to the model values using (7) for the average parameters (solid light gray curve with squares in Figure 9) or (8) (dotted light gray curve with squares in Figure 9). But during the second and third days after the onset of low Kp (third and fourth data points in Figure 9), the log average $\rho_{m,eq}$ based on all the data (black curve) rises significantly above that of the models (light gray curves). This indicates that on average there is apparent refilling during quiet intervals. Note that the Kp-dependent model (dotted light gray curve with

squares in Figure 9) does predict some apparent refilling, but not enough to explain the data.

Considering that $\rho_{\mathrm{m,eq}}$ is greater at solar maximum than at solar minimum (e.g., comparing $\rho_{\mathrm{m,eq}}$ in the lower panels of Figure 8 to $\rho_{\mathrm{m,eq}}$ in the upper panels), it would not be surprising if the apparent refilling is different at solar maximum from that at solar minimum, and this is the case. The red curve with upward pointing triangles in Figure 9 shows the log average of $\rho_{\mathrm{m,eq}}$ during the same four daily intervals, but computing the average only of the data with F10.7 $>$ 150 sfu, characteristic of solar maximum. On the other hand, the blue curve with downward pointing triangles in Figure 9 is calculated only using data with F10.7 $<$ 100 sfu, characteristic of solar minimum. In Figure 9, the red curve starts out at higher values of $\rho_{\mathrm{m,eq}}$ and rises relatively less than the average of all data (black curve), while the blue curve starts out at lower values of $\rho_{\mathrm{m,eq}}$ and rises relatively more than the average of all data (black curve).

The three black or blue data points within the interval of low Kp (three data points to the right of the vertical gray line in Figure 9) lie almost along a straight line using a log scale (Figure 9b). This suggests exponential growth. Despite the fact that the three red points do not lie on a straight line, we will characterize all three curves by the slope between the first and third data points. We find then

$$\frac{d\log_{10}(\rho_{\mathrm{m,eq}})}{dt} = 0.27 \text{ day}^{-1}, \text{ for all data,} \quad (11)$$

$$= 0.16 \text{ day}^{-1}, \text{ for F10.7} > 150 \text{ sfu,} \quad (12)$$

$$= 0.35 \text{ day}^{-1}, \text{ for F10.7} < 100 \text{ sfu,} \quad (13)$$

5. Discussion and Summary

For this study, we used the inferred equatorial mass density $\rho_{\mathrm{m,eq}}$ based on measurements of Alfvén wave frequencies measured by the GOES satellites during 1980–1991 along with a model for the field line dependence based on the same data set [*Denton et al.*, 2015]. Using this data, we constructed a number of different models for the equatorial mass density at geostationary orbit (Section 3). The most complicated model with or without Kp dependence, (7) or (8), respectively, is able to account for 66% of the variance with a typical variation from actual values of a factor of 1.56. We also described some simpler models.

Of the factors influencing $\rho_{\mathrm{m,eq}}$ that we considered, the most important factor is the F10.7 EUV index. This presumably acts by increasing the ionospheric temperature and raising the scale height of the ions, making it easier for ions to overcome gravity and rise to the magnetic equator, especially for O+ that disproportionately affects ρ_{m} because of its high ion mass. Other factors may also be involved in getting O+ up to the equatorial magnetosphere, but increased ionospheric temperature certainly facilitates the process.

Mass accumulates as flux tubes convect eastward from midnight local time toward the afternoon local time sector, apparently because of continued refilling along the drift paths that extend eastward from the nightside magnetosphere to the afternoon local time sector. A drop in $\rho_{\mathrm{m,eq}}$ after dusk may occur because the high mass plasma is convected on open drift paths out toward the magnetopause [*Denton et al.*, 2014b].

The mass density is larger for larger solar wind dynamic pressure P_{dyn}. While we don't have a detailed explanation for this process, certainly increasing P_{dyn} leads to greater geomagnetic activity that could possibly lead to more mass.

There is a small dependence of $\rho_{\mathrm{m,eq}}$ on the phase of the year, indicating a seasonal effect. The mass density is greatest at a fraction of about 0.052 into the year, corresponding approximately to January 20, that is, the winter solstice. We don't currently have any explanation of this dependence. It is at most a factor of $10^{0.08} = 1.20$ (equation (7)).

There is also a small dependence of $\rho_{\mathrm{m,eq}}$ on the solar wind B_Z. Positive B_Z is more likely to lead to a closed magnetosphere in which refilling can more easily occur.

Our model accounts for much of the variation in $\rho_{\mathrm{m,eq}}$, but even the Kp-dependent model does not account well for refilling during extended geomagnetically quiet intervals. We need a better understanding of the factors that contribute to large $\rho_{\mathrm{m,eq}}$.

For 10 especially quiet intervals, we considered long-term (> 1 day) apparent refilling. We emphasize that apparent refilling is not necessarily refilling of the same flux tube. We found that the behavior of $\rho_{\mathrm{m,eq}}$ varies for different events. In some cases, there is significant apparent refilling, whereas in other cases $\rho_{\mathrm{m,eq}}$ stays the same or even decreases slightly.

Nevertheless, we showed that on average $\rho_{\mathrm{m,eq}}$ increases exponentially during quiet intervals. At solar maximum, the value of $\rho_{\mathrm{m,eq}}$ is larger at the beginning of the quiet interval, and the subsequent apparent refilling rate is less than that of all the data combined. On the other hand, at solar minimum, the value of $\rho_{\mathrm{m,eq}}$ is lower at the beginning of the quiet interval, and the subsequent apparent refilling rate is greater than that of all the data combined. On the third day of apparent refilling, the difference in $\rho_{\mathrm{m,eq}}$ at solar maximum or solar minimum is small compared to the difference in $\rho_{\mathrm{m,eq}}$ at the beginning of the quiet interval.

Global MHD models are only now starting to incorporate plasmaspheric plasma into simulations. When the only source of plasma comes from the solar wind, the simulation $\rho_{\mathrm{m,eq}}$ is much lower than realistic. The models and refilling rates that we have described here are a starting point toward developing radially dependent models for $\rho_{\mathrm{m,eq}}$ that can be used to construct more realistic plasmasphere models for use in MHD codes. A study like this one, but incorporating radial variation, would help to achieve this goal.

Acknowledgments. Work at Dartmouth was supported by NSF grant AGS-1105790 and NASA grant NNX10AQ60G. Work at JHU APL was supported by NSF Grant AGS-1106427. Solar wind parameters and geomagnetic indices were obtained from the GSFC/SPDF OMNIWeb interface at http://omniweb.gsfc.nasa.gov. The *Kondrashov et al.* [2014] database was used to fill in missing values during data gaps (http://onlinelibrary.wiley.com/doi/10.1002/2014GL059741/full). Values of F10.7 come originally from NOAA's National Geophysical Data Center. Numerical data shown in this paper are available from the lead author upon request.

References

Bame, S. J., et al. (1993), Magnetospheric plasma analyzer for spacecraft with constrained resources, *Review of Scientific Instruments*, *64*(4), 1026–1033.

Benson, R. F., P. A. Webb, J. L. Green, L. Garcia, and B. W. Reinisch (2004), Magnetospheric electron densities inferred from upper-hybrid band emissions, *Geophys. Res. Lett.*, *31*(20), doi:10.1029/2004gl020847.

Berube, D., M. B. Moldwin, S. F. Fung, and J. L. Green (2005), A plasmaspheric mass density model and constraints on its heavy ion concentration, *J. Geophys. Res.*, *110*(A4),

A04212, doi:10.1029/2004JA010684.

Denton, M. H., V. K. Jordanova, M. G. Henderson, R. M. Skoug, M. F. Thomsen, C. J. Pollock, S. Zaharia, and H. O. Funsten (2005), Storm-time plasma signatures observed by image/mena and comparison with a global physics-based model, *Geophys. Res. Lett.*, *32*(17), l17102, doi:10.1029/2005gl023353.

Denton, R. E. (2006), Magneto-seismology using spacecraft observations, in *Magnetospheric ULF waves: Synthesis and new directions*, edited by K. Takahashi, P. J. Chi, R. E. Denton, and R. L. Lysak, Geophysical monograph, pp. 307–317, American Geophysical Union, Washington, DC, english.

Denton, R. E., K. Takahashi, I. A. Galkin, P. A. Nsumei, X. Huang, B. W. Reinisch, R. R. Anderson, M. K. Sleeper, and W. J. Hughes (2006), Distribution of density along magnetospheric field lines, *J. Geophys. Res.*, *111*(A4), A04213, doi:10.1029/2005JA011414.

Denton, R. E., M. F. Thomsen, K. Takahashi, R. R. Anderson, and H. J. Singer (2011), Solar cycle dependence of bulk ion composition at geosynchronous orbit, *J. Geophys. Res.*, *116*, a03212, doi:10.1029/2010ja016027.

Denton, R. E., Y. Wang, P. A. Webb, P. M. Tengdin, J. Goldstein, J. A. Redfern, and B. W. Reinisch (2012), Magnetospheric electron density long-term (> 1 day) refilling rates inferred from passive radio emissions measured by image rpi during geomagnetically quiet times, *J. Geophys. Res.*, *117*, a03221, doi:10.1029/2011ja017274.

Denton, R. E., V. K. Jordanova, and B. J. Fraser (2014a), Effect of spatial density variation and O+ concentration on the growth and evolution of electromagnetic ion cyclotron waves, *J. Geophys. Res.*, *119*(10), 8372–8395, doi:10.1002/2014ja020384.

Denton, R. E., K. Takahashi, M. F. Thomsen, J. E. Borovsky, H. J. Singer, Y. Wang, J. Goldstein, P. C. Brandt, and B. W. Reinisch (2014b), Evolution of mass density and O+ concentration at geostationary orbit during storm and quiet events, *J. Geophys. Res.*, *119*(8), doi:10.1002/2014ja019888.

Denton, R. E., K. Takahashi, J. Lee, C. K. Zeitler, N. T. Wimer, L. E. Litscher, H. J. Singer, and K. Min (2015), Field line distribution of mass density at geostationary orbit, *J. Geophys. Res.*, *120*(6), 4409–4422, doi:10.1002/2014ja020810.

Kondrashov, D., R. Denton, Y. Y. Shprits, and H. J. Singer (2014), Reconstruction of gaps in the past history of solar wind parameters, *Geophys. Res. Lett.*, *41*(8), 2702–2707, doi:10.1002/2014gl059741.

Newell, P. T., T. Sotirelis, K. Liou, C. I. Meng, and F. J. Rich (2007), A nearly universal solar wind-magnetosphere coupling function inferred from 10 magnetospheric state variables, *J. Geophys. Res.*, *112*(A1), a01206, doi:10.1029/2006ja012015.

Persoon, A. M., D. A. Gurnett, and S. D. Shawhan (1983), Polar cap electron densities from DE-1 plasma wave observations, *J. Geophys. Res.*, *88*(NA12), 123–136, doi:10.1029/JA088iA12p10123.

Qin, Z., R. E. Denton, N. A. Tsyganenko, and S. Wolf (2007), Solar wind parameters for magnetospheric magnetic field modeling, *Space Weather*, *5*(11), S11003, doi:10.1029/2006SW000296.

Schmidt, M., and H. Lipson (2009), Distilling free-form natural laws from experimental data, *Science*, *324*(5923), 81–85, doi:10.1126/science.1165893.

Singer, H. J., D. J. Southwood, R. J. Walker, and M. G. Kivelson (1981), Alfven-wave resonances in a realistic magnetospheric magnetic-field geometry, *J. Geophys. Res.*,

437 *86*(NA6).

438 Takahashi, K., R. E. Denton, and H. J. Singer (2010), Solar cycle variation of geosyn-
439 chronous plasma mass density derived from the frequency of standing alfven waves, *J.*
440 *Geophys. Res.*, *115*, doi:10.1029/2009ja015243.

441 Tsyganenko, N. A., and M. I. Sitnov (2005), Modeling the dynamics of the inner
442 magnetosphere during strong geomagnetic storms, *J. Geophys. Res.*, *110*(A3), doi:
443 10.1029/2004ja010798.

444 Waters, C. L., F. W. Menk, M. F. Thomsen, C. Foster, and F. R. Fenrich (2006), Remote-
445 sensing the magnetosphere using ground-based observations of ULF waves, in *Magne-*
446 *tospheric ULF Waves: Synthesis and New Directions*, edited by K. Takahashi, P. J.
447 Chi, R. E. Denton, and R. L. Lysak, Geophysical Monograph, pp. 319–340, American
448 Geophysical Union, Washington D.C.

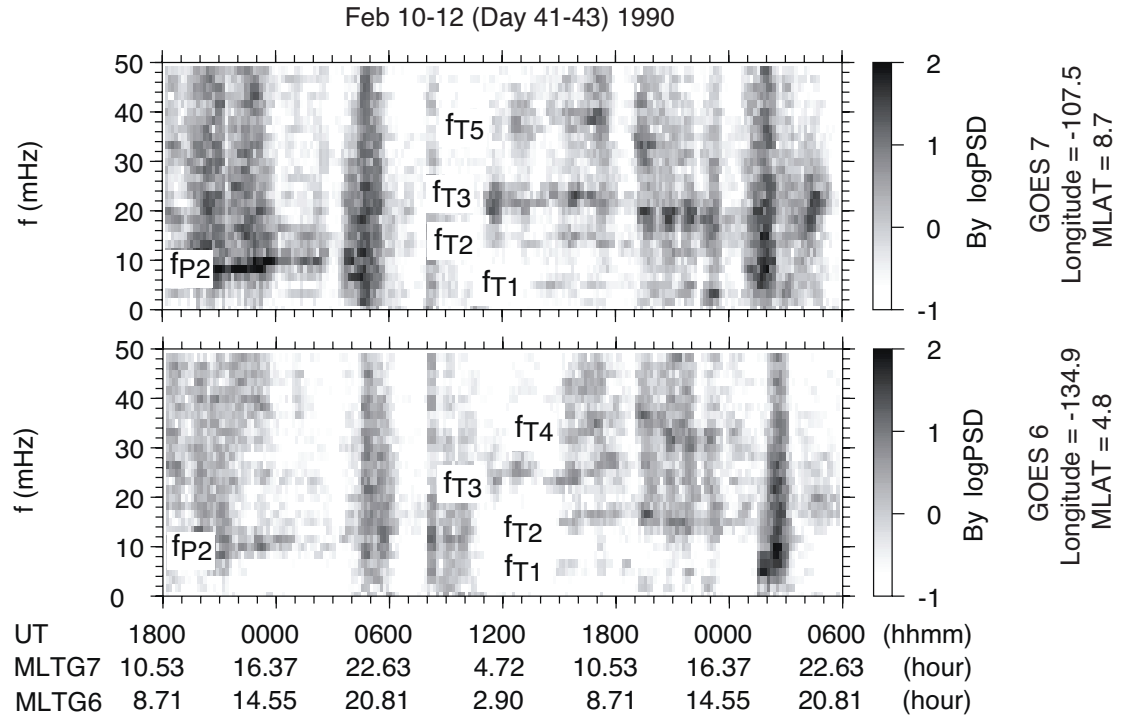

Figure 1. Dynamic spectra of the azimuthal component of the magnetic field, B_y observed by (bottom) GOES 6 and (top) GOES 7 for a 36 h period centered on 1200 UT of day of year (DOY) 42 (11 February 1990). Visible toroidal harmonics are labeled "fT1" through "fT5". The isolated strong spectral line labeled "fP2" is attributed to the second harmonic poloidal wave [Cummings et al., 1969], based on the even stronger power in the B_x component (not shown). The MLT value for each satellite is shown at the bottom. (Reproduced from Figure 3 of *Takahashi et al.* [2010])

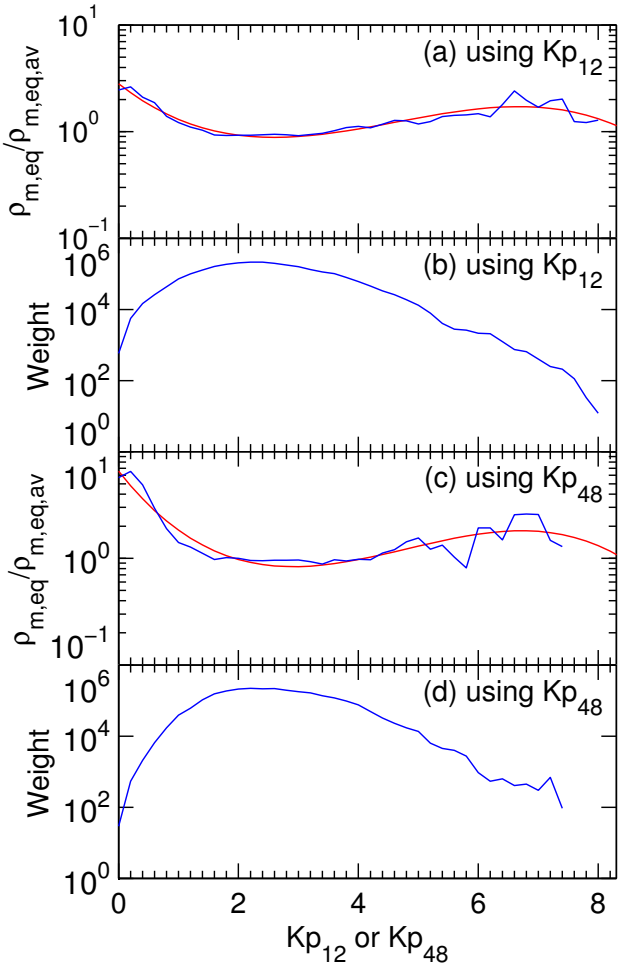

Figure 2. (a) Binned values of $\rho_{\mathrm{m,eq}}$ divided by the weighted log average of $\rho_{\mathrm{m,eq}}$, $\rho_{\mathrm{m,eq,av}}$, and (b) weight in bins of width 0.2 versus Kp_{12}; (c) and (d) are the same as (a) and (b), except using Kp_{48}.

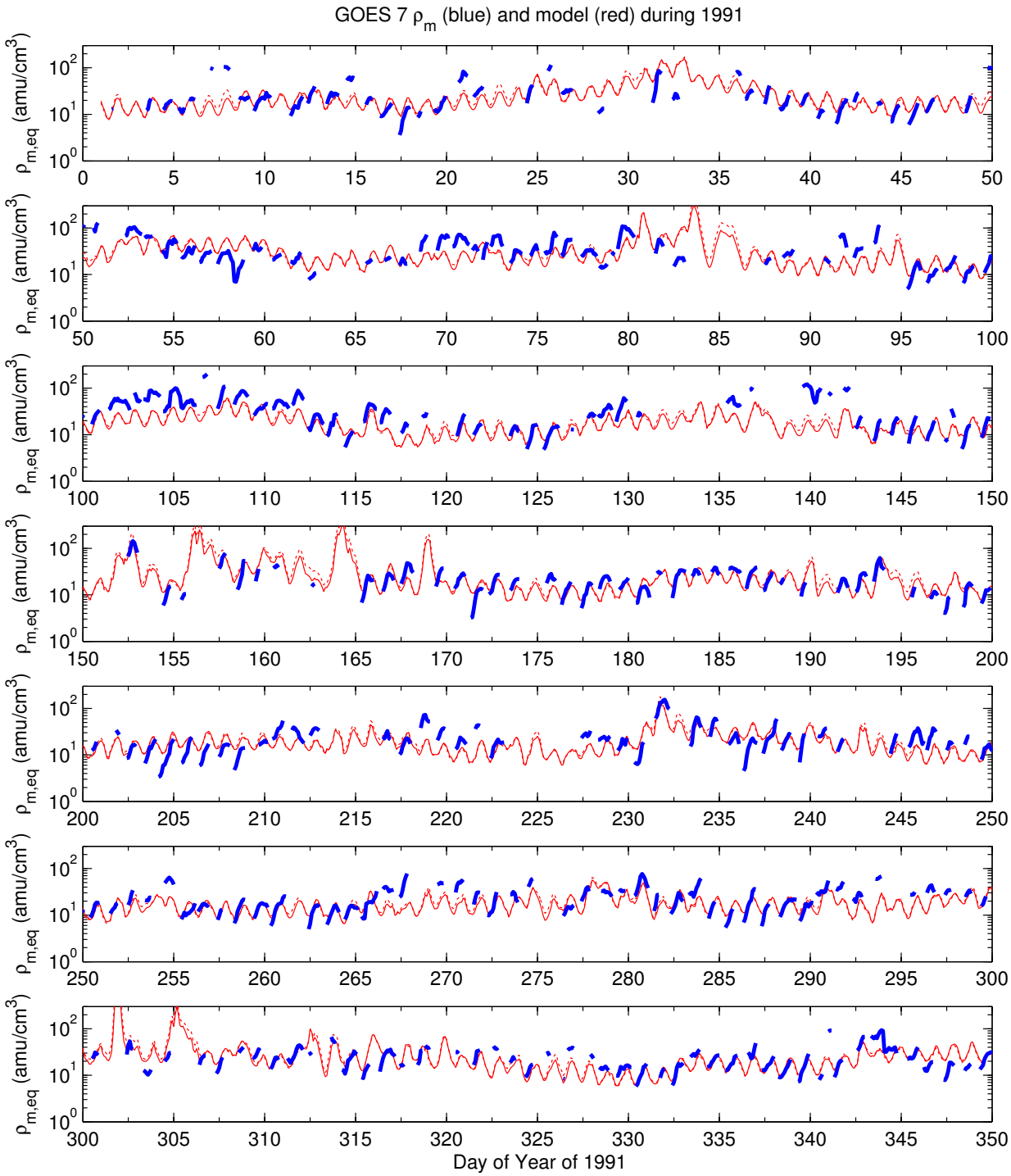

Figure 3. Mass density inferred from Alfvén waves measured by GOES 7 (thick blue curves) and that given by the most detailed model without Kp dependence (7) (solid red curves) and the model with Kp dependence (8) (dotted red curves) during 1991 versus day of year (DOY).

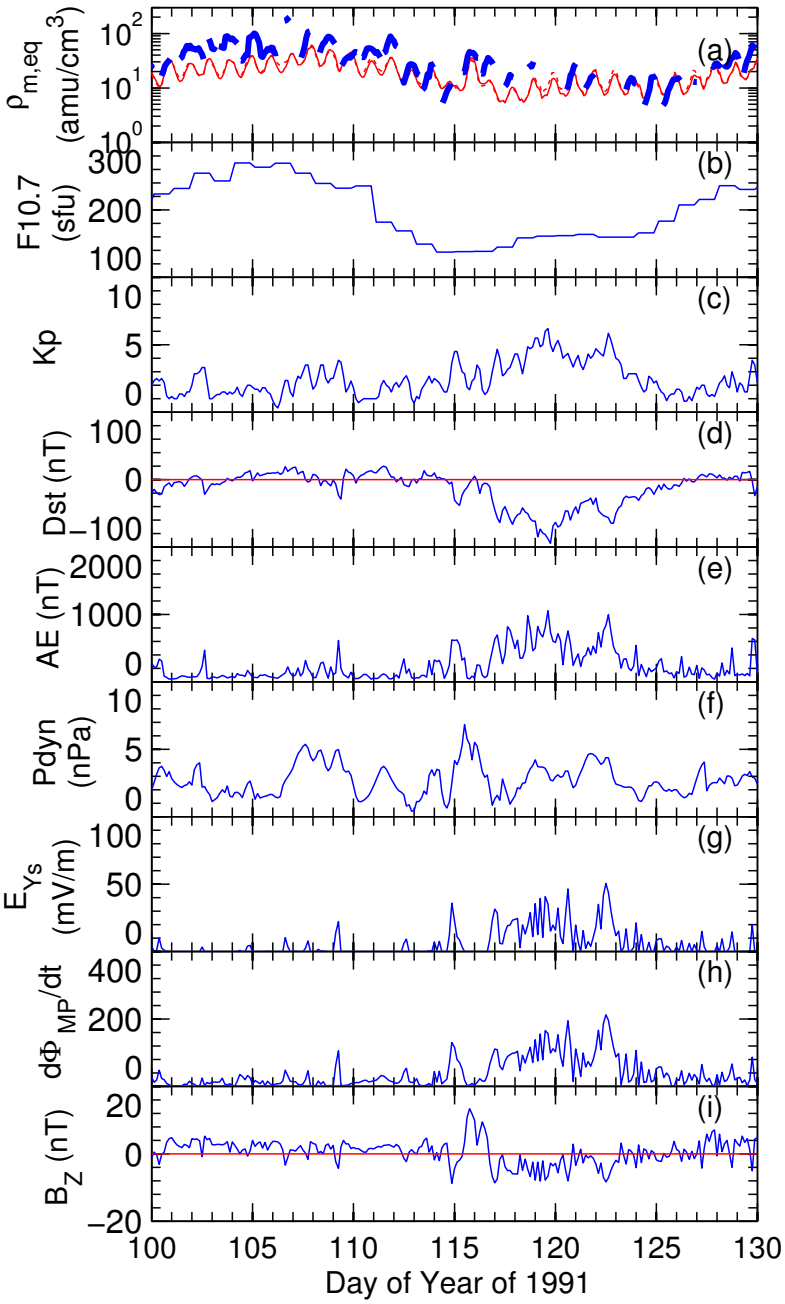

Figure 4. (a) Mass density inferred from Alfvén waves measured by GOES 7 (thick blue curves) and that given by the most detailed model without Kp dependence (7) (solid red curves) and the model with Kp dependence (8) (dotted red curves) versus day of year (DOY) 100 to 130 during 1991. Panels (b) through (i) show instantaneous values of various geomagnetic indices and solar wind parameters as described in the text (blue curves). The red horizontal lines are at a value of zero.

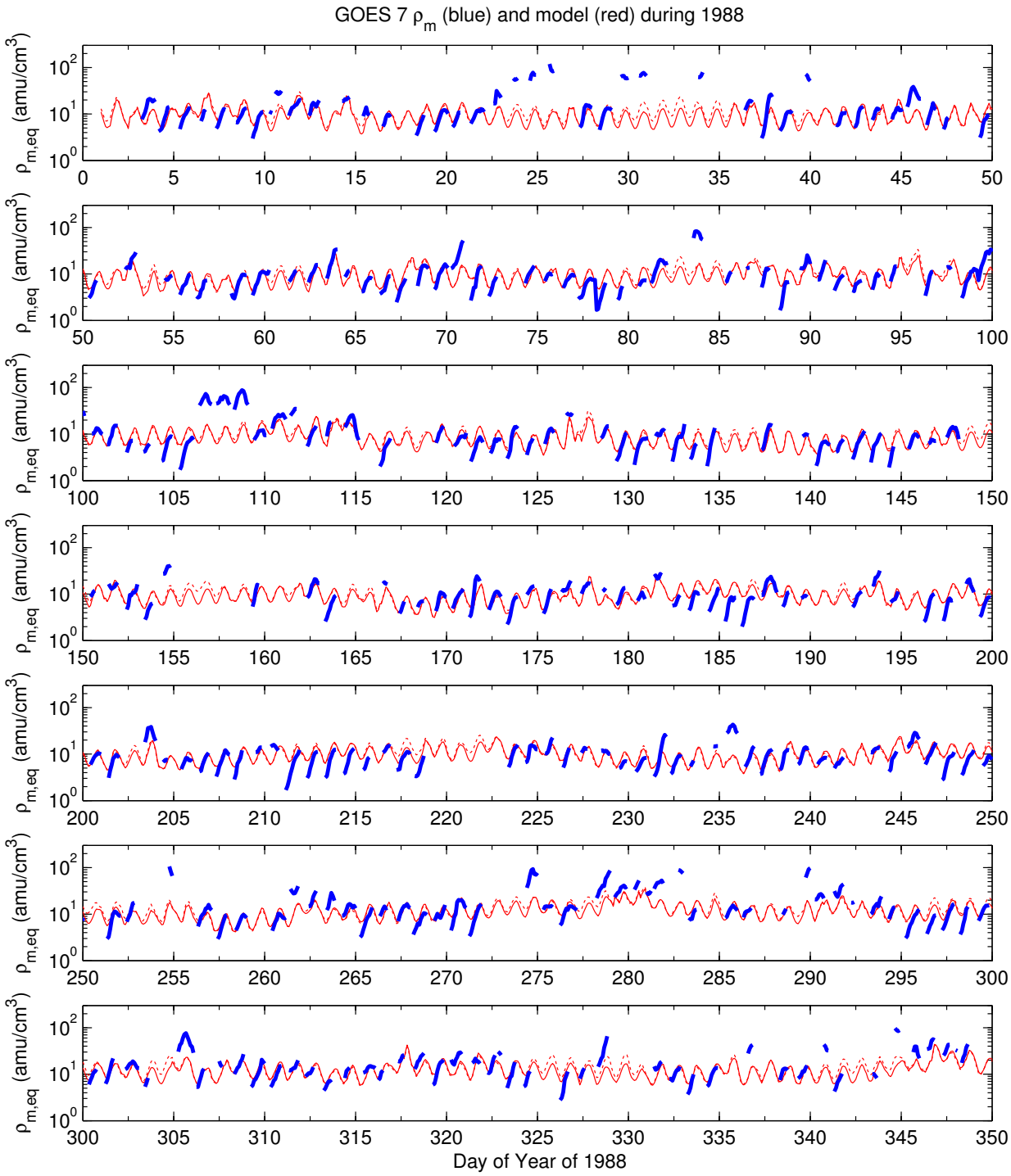

Figure 5. Similar to Figure 3, but for 1988.

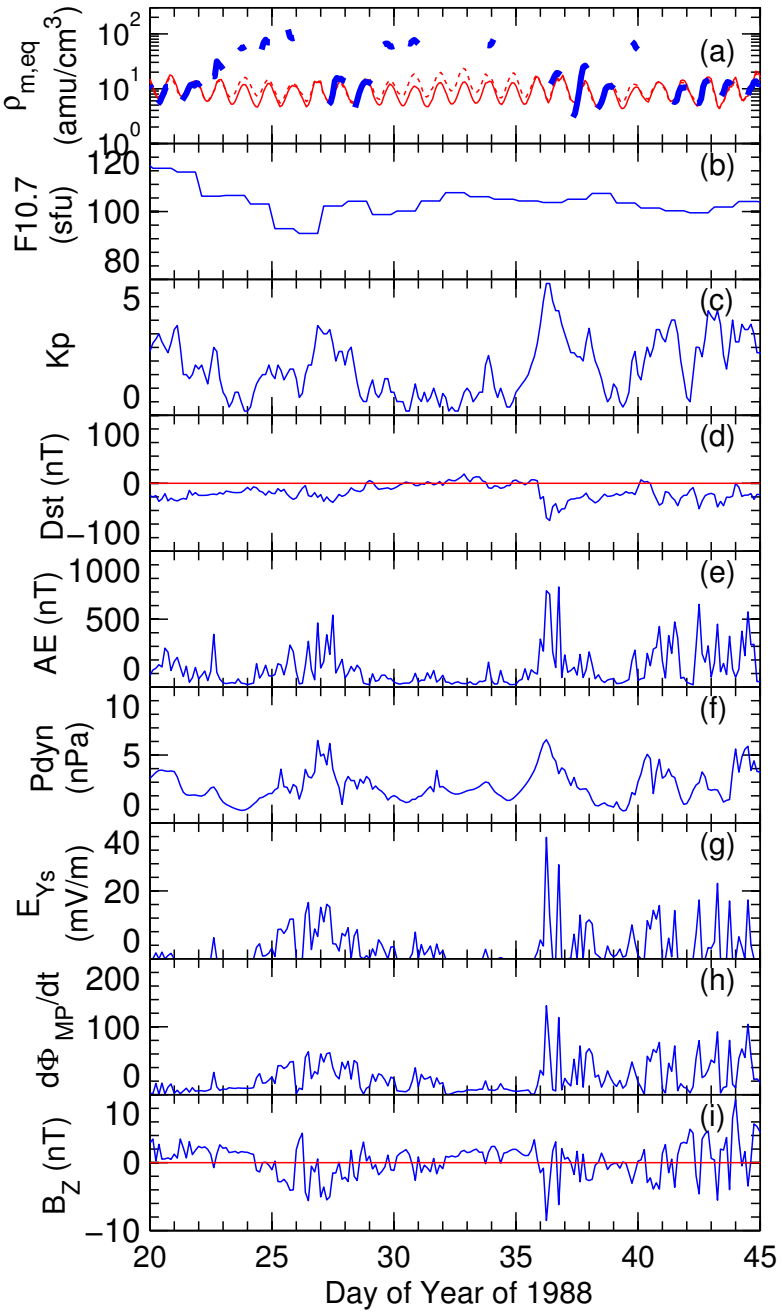

Figure 6. Similar to Figure 4, but for DOY 20 to 45 during year 1988.

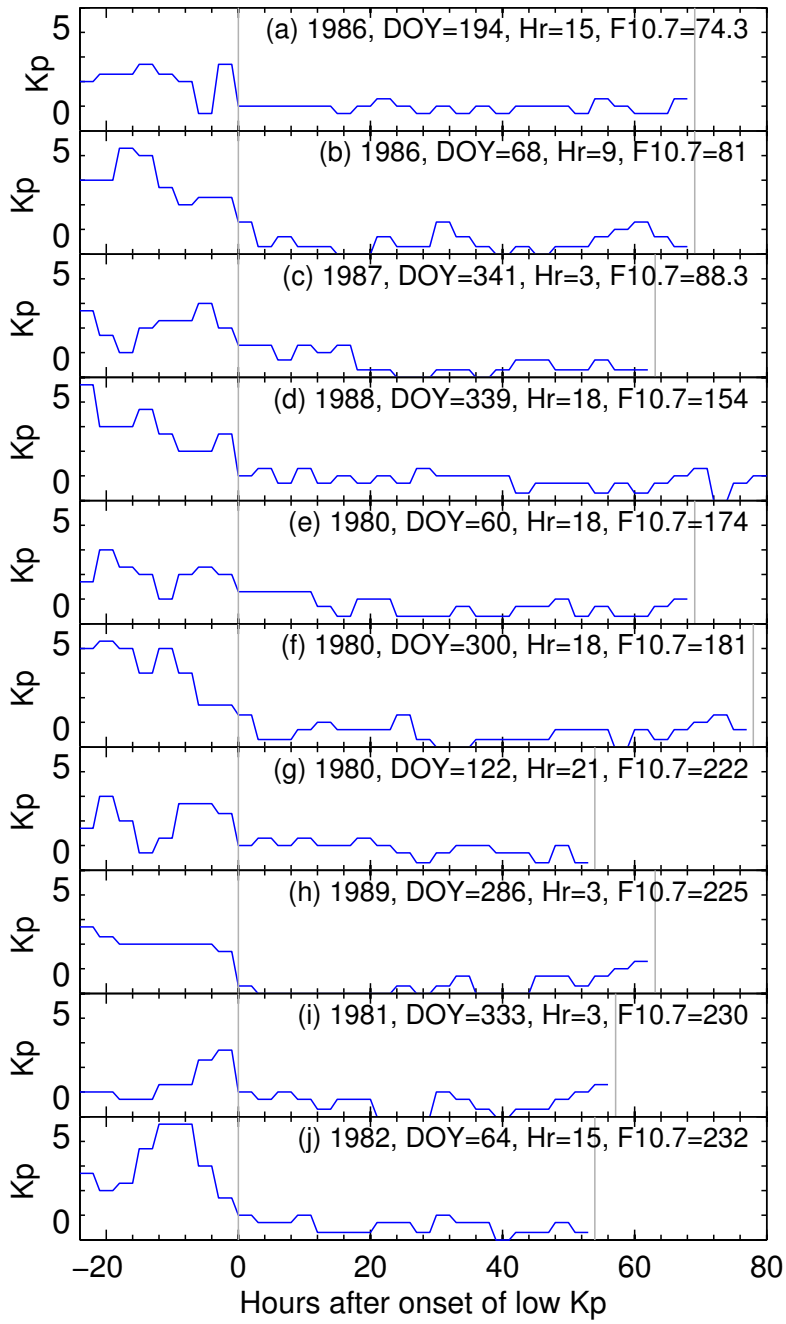

Figure 7. Kp (interpolated to hourly values) versus hours after the beginning of the period of low Kp for the 10 events, as described in the text. The two vertical gray lines mark the beginning of the period of low Kp (leftmost gray vertical line) and the end of that period (rightmost gray vertical line).

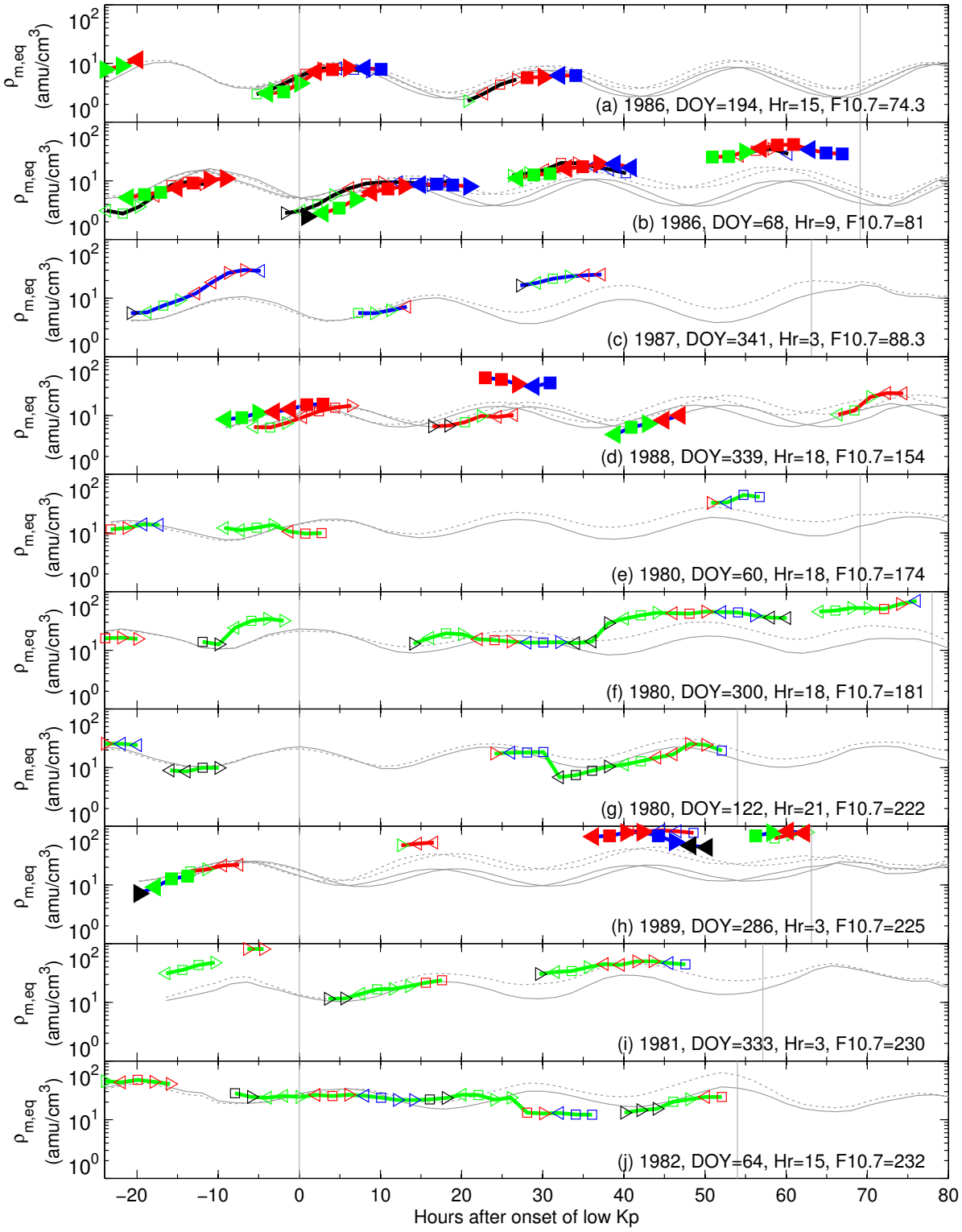

Figure 8. Inferred equatorial mass density at GOES (colored symbols and curves) and model mass density using (7) (solid light gray curves) and (8) (dotted light gray curves) versus hours after onset of low Kp for each of the events shown in Figure 7. The data points (colored symbols) are two hour log average values with red color for MLT centered on 10, 12, and 14 hr, blue color for MLT centered on 16, 18, and 20 hr, black color for MLT centered on 22, 0, and 2 hr, and green color for MLT centered on 4, 6, and 8 hr.

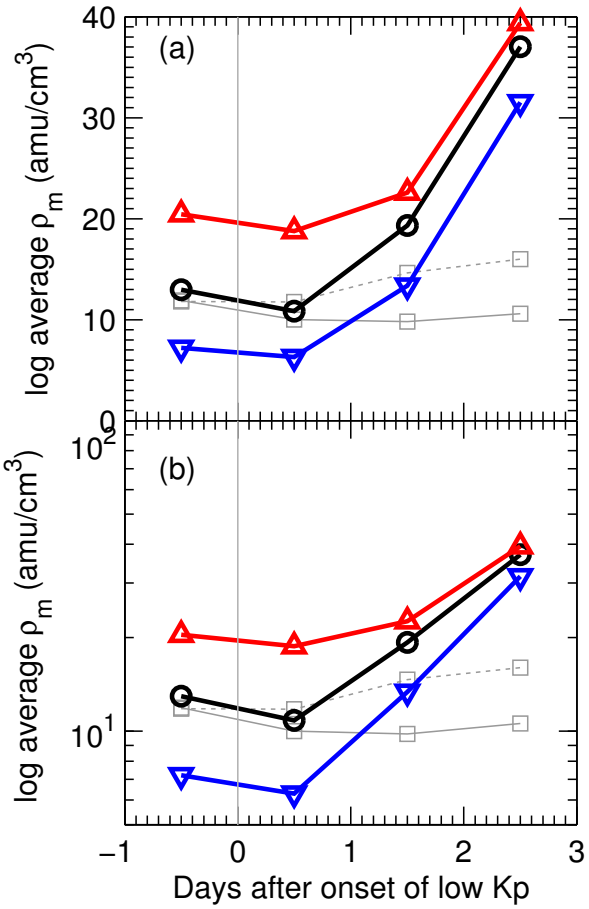

Figure 9. Log average daily mass density versus days after onset of low Kp (vertical gray line) using a (a) linear or (b) log scale. The black curve with circles shows the log average of all the data, the red curve with upward pointing triangles shows the average of the data with F10.7 > 150 sfu (solar max), and the blue curve with downward pointing triangles shows the average of the data with F10.7 < 100 sfu (solar min). The light gray curves with squares shows the model values using (7) (solid light gray curve) or (8) (dotted light gray curve) for the average parameters.